

## G12AC20042 Final Technical Report

# High resolution mapping of active faults and earthquakes using topography derived from lidar

Edwin Nissen

Department of Geophysics, Colorado School of Mines, Golden CO 80401

2/15/2012–8/14/2014

## Abstract

We investigate shallow slip in the 4 April 2010 El Mayor-Cucapah (Mexico) earthquake using three-dimensional surface deformation computed from pre- and post-event airborne light detection and ranging (lidar) topography. Focusing on the northern part of the rupture zone, we seek to resolve a discrepancy between fault models based upon field observations, which implicate low-angle, NE-dipping detachment faults, and those based upon space geodetic and seismological data, which support slip on sub-vertical structures. By resolving the three-dimensional lidar displacements into vertical, fault trace-parallel (NW- or SE-directed) and fault trace-normal (NE- or SW-directed) components, we are able to test these models explicitly. Along most of the fault trace, we find that the vertical throw accommodated by the surface rupture far exceeds the extensional heave, indicating that coseismic faulting at depth is steeply-dipping. However, the heave exceeds the throw along a short (<5 km) section of the Paso Superior fault, hinting that a low-angle structure may have been reactivated locally, at least within the relatively narrow extents of the lidar footprint. The differencing methods developed as part of this award exploit airborne lidar in this instance, but in principal could be applied to any kind of high-resolution topography data, including those generated by state-of-the-art satellite or aerial stereo-photogrammetric methods.

## 1 Introduction

Mapping the spatial distribution of slip in an earthquake is important for determining the frictional and rheological properties of the fault zone, charting the transfer of stresses onto neighbouring faults, and interpreting the long-term record of earthquakes recorded in landscapes. Interferometric Synthetic Aperture Radar (InSAR) and cross-correlation of optical or SAR amplitude images are the prevalent geodetic techniques for mapping surface deformation over large areas ( $\sim 10^2$ – $10^4$  km<sup>2</sup>) at high spatial resolution ( $\sim 10^0$ – $10^2$  m). Yielding displacements in the satellite line-of-sight and horizontal directions, respectively, InSAR and image cross-correlation methods must therefore be used in combination in order to capture the full three-dimensional (3-D) deformation field. Furthermore, InSAR coverage is often limited by decorrelation close to the fault surface trace caused by steep phase gradients and secondary effects such as landsliding, while optical image cross-correlation can similarly break down in areas of rapid vegetation growth or agricultural change.

The increased availability of sub-meter resolution topography derived from airborne light detection and ranging (lidar) or stereo-photogrammetry offers a potential way round these limitations.

An explosion of lidar surveying along major faults in the western United States and some other tectonically-active regions in the past decade has generated many new opportunities for studying past earthquakes and tectonic geomorphology, but also provides a high-resolution baseline against which future topography data — such as those collected after an earthquake — can be compared. Because the slip in large earthquakes is greater than the sub-meter point spacing typical of lidar, differencing ‘before’ and ‘after’ topography can potentially resolve dense, 3-D earthquake displacements along these faults, including in the near-fault region where InSAR usually breaks down, and in highly vegetated areas where C-band InSAR and pixel cross-correlation may struggle. However, methods for deriving 3-D coseismic displacements from topographic differencing are currently at a nascent stage of development, with only a few real case studies on which to test them.

This project has supported advances in 3-D displacement measurement techniques and their application to some of the earliest earthquakes to be captured by ‘before’ and ‘after’ lidar data. Presented in this technical report is an analysis of one of these case studies, the  $M_w$  7.2 El Mayor-Cucapah (Mexico) earthquake of 4 April 2010. This case study will demonstrate two of the key advantages that topography differencing provides: (1) the ability to calculate surface displacements in three dimensions, and (2) the potential to resolve coherent displacements within a highly-deformed fault zone. Our central interest in the El Mayor-Cucapah earthquake is in the correspondence between shallow fault zone deformation and mapped surface offsets, which include rare observations and inferences of oblique right-lateral and normal slip on a low-angle ( $\sim 20^\circ$ -dipping) detachment fault (Fletcher *et al.*, 2014; Teran *et al.*, 2015). The implication of low-angle slip is inconsistent with earthquake source models based on space geodesy and seismology which support steeply-dipping or sub-vertical faulting (Fialko *et al.*, 2010; Hauksson *et al.*, 2011; Wei *et al.*, 2011; Zheng *et al.*, 2012; Uchide *et al.*, 2013).

Resolving this discrepancy is important for the long-standing debate over whether low-angle normal faults host large earthquakes (e.g. Proffett, 1977; Abers, 1991; Jackson and White, 1989; Wernicke, 1995; Axen, 1999; Styron and Hetland, 2014). It also has regional implications for how oblique extension is accommodated along this section of the Pacific-North America plate boundary (Axen *et al.*, 1999; Nagy and Stock, 2000; Fletcher and Spelz, 2009; Mueller *et al.*, 2009). Finally, the mechanism of the El Mayor-Cucapah earthquake has an important bearing on stresses transferred to neighboring faults; for instance, normal slip on a shallow-angle, NE-dipping detachment could lead to a significant reduction of clamping stresses on the Imperial and San Jacinto faults to the NE (Figure 1a).

This work has been a collaborative effort with scientists from several universities, which has been further supported through separate but related grants from the National Science Foundation and the Southern California Earthquake Center (see Acknowledgements). We have already published a paper discussing the challenges in processing the El Mayor-Cucapah lidar data in Glennie *et al.* (2014), and this Final Report instead focuses on the tectonic implications of these results. This analysis has been shaped by conversations with colleagues but any mistakes or misrepresentations are my own. This award also helped support work on two Japanese case studies, which better demonstrate the possibility of mapping ground deformation in the presence of dense vegetation (Nissen *et al.*, 2014).

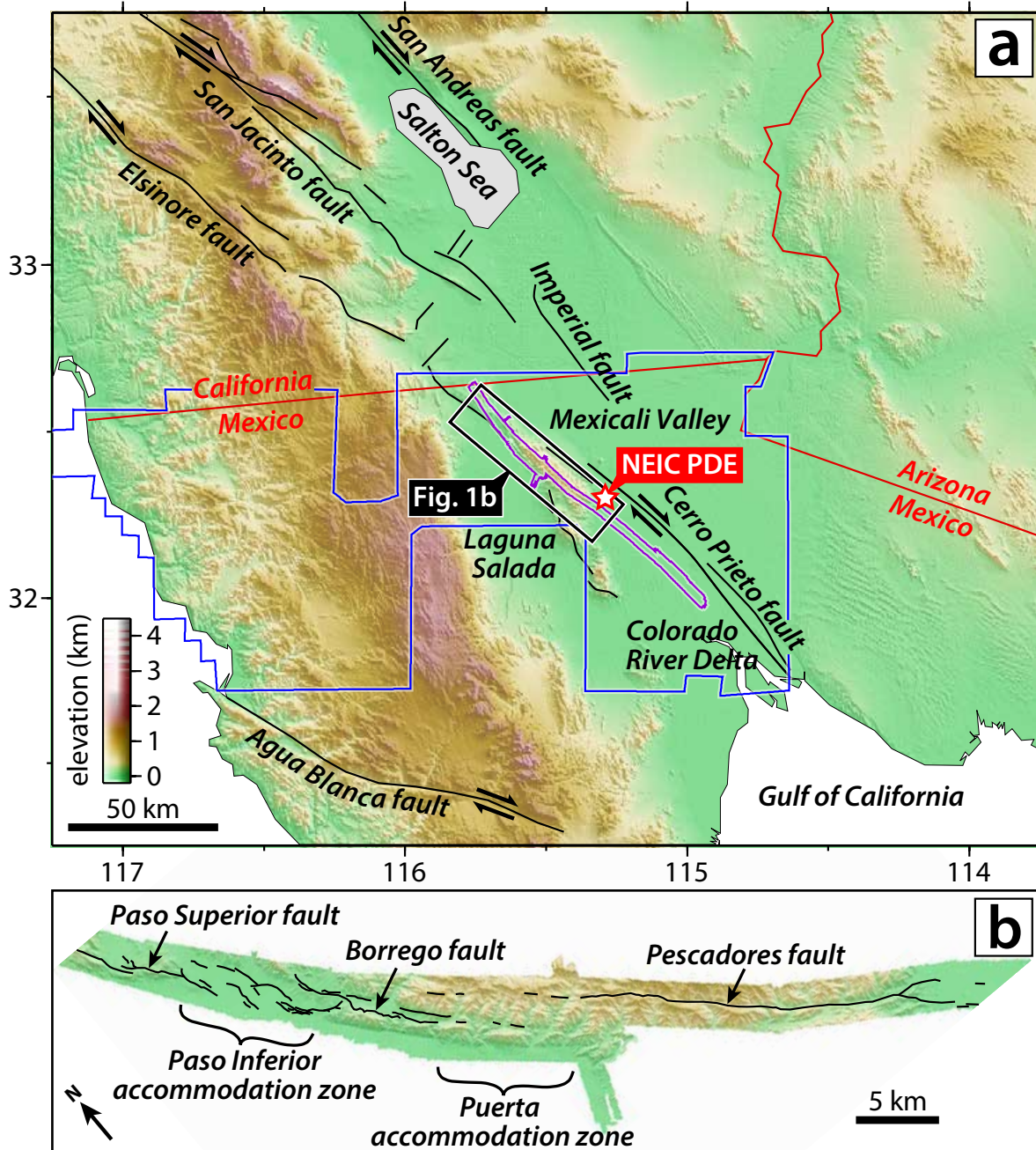


Figure 1: (a) Tectonic setting of the 4 April 2010 El Mayor-Cucapah earthquake. The blue polygon represents pre-event lidar survey extents and the magenta polygon shows the extents of the post-event lidar survey, which captures the 2010 surface rupture. The red star is the Preliminary Determined Epicenter from the USGS National Earthquake Information Center. (b) Post-event lidar topography in the Sierra Cucapah, with mapped surface ruptures from Fletcher et al. (2014). This figure is modified from Glennie et al. (2014).

## 2 The El Mayor-Cucapah earthquake

The El Mayor-Cucapah earthquake struck northern Baja California, Mexico, at 22:40 UTC on 4 April 2010, causing major damage to Mexicali and Calexico, killing four people and injuring around 100 (Figure 1a). Its epicenter was situated at the southeastern end of the NW-SE-trending Sierra Cucapah range and at the northern end of the N-S-trending Sierra El Mayor range. These mountain belts separate the low-lying Mexicali Valley to the NE from the Laguna Salada basin to the SW. This region forms part of the Pacific–North American plate boundary zone, which accommodates  $\sim 5$  cm/yr of NW-SE right-lateral shear at this latitude. How this overall plate boundary strain rate is distributed amongst major faults in the region is currently poorly understood.

### 2.1 Observations from seismology

A double-couple focal mechanism calculated from  $P$ -wave first motions indicates oblique slip on moderate angle E-dipping (normal/left-lateral) or SW-dipping (normal/right-lateral) planes (*Uchide et al.*, 2013), whereas solutions determined from regional long-period seismograms show predominantly strike-slip motion on sub-vertical NW-SE and NE-SW-striking nodal planes, with a non-double couple component that is consistent with additional NW-SE-striking normal faulting (*Hauksson et al.*, 2011). Regional high-rate GPS displacements support an almost pure strike-slip mechanism on sub-vertical planes (*Zheng et al.*, 2012). Aftershocks relocated using double difference techniques form a  $\sim 120$  km-long,  $\sim 10$  km-wide band that extends northwest of the hypocenter along the Sierra Cucapah range and south-east of it across the Colorado river delta, with maximum hypocenter depths of 15–20 km and mechanisms that generally mimic the mainshock long-period moment tensor (*Hauksson et al.*, 2011; *Castro et al.*, 2011).

### 2.2 Observations from satellite geodesy

Coseismic surface deformation was initially mapped using satellite imagery, prior to the detailed field and lidar analyses described in the following subsection. Line-of-sight displacements measured with Interferometric Synthetic Aperture Radar (InSAR) and horizontal displacements from sub-pixel correlation of optical and SAR amplitude images revealed faulting extending along the full length of the main aftershock zone, from the the Colorado river delta in the SE, through the interior of the Sierra Cucapah range, to the US–Mexico border in the NW (*Fialko et al.*, 2010; *Wei et al.*, 2011).

On close inspection the rupture trace incorporates several discrete faults segments. From SE to NW, these are the Indiviso fault within the Colorado River delta (which had not previously been recognized), and the Laguna Salada, Pescadores, Borrego, and Paso Superior faults within the Sierra Cucapah mountains (which were mapped but mostly considered inactive before this earthquake). A surprising aspect of the earthquake is that it ruptured into stress shadows of recent events on adjacent, parallel faults (*Fialko et al.*, 2010; *Fletcher et al.*, 2014). The surface traces of the Paso Superior and Borrego faults lie within 1–2 km of the northern (W-dipping) Laguna Salada fault along the western Sierra Cucapah range-front, which ruptured in a  $M \sim 7.2$  earthquake in 1892 (*Mueller and Rockwell*, 1995; *Hough and Elliot*, 2004). The Indiviso fault lies  $\sim 10$  km SW of the Cerro Prieto fault which hosted  $M \sim 7.1$ ,  $\sim 6.1$  and  $\sim 5.4$  earthquakes in 1934, 1980 and 2006, respectively (*Suárez-Vidal et al.*, 2007). However, fluid extraction in the Cerro Prieto geothermal field,  $\sim 15$  km NE of the El Mayor-Cucapah epicenter, may have reduced the stress shadowing from these prior events and promoted triggering of the 2010 earthquake (*Trugman et al.*, 2014).

Analysis of InSAR line-of-sight displacements, horizontal satellite pixel offsets, and regional GPS velocities supports steeply-dipping to sub-vertical faulting, in agreement with the seismological moment tensor solutions. An elastic dislocation model by *Fialko et al.* (2010), published also in *Gonzalez-Ortega et al.* (2014), indicates a  $71^\circ$  NE-ward dip for the Paso Superior and Borrego faults, a  $79^\circ$  NE-ward dip for the Pescadores fault, and  $59^\circ$  and  $89^\circ$  SW-ward dips along Indiviso fault. An alternative model by *Wei et al.* (2011) shows a  $50^\circ$  NE-ward dip for the Paso Superior fault, a  $75^\circ$  NE-ward dip for the Borrego and Pescadores faults, and a  $60^\circ$  SW-ward dip for the Indiviso fault. Their model also invokes slip on a  $45^\circ$ , E-dipping normal fault at the southern end of the Sierra Cucapah, which corresponds to the earthquake hypocenter and accounts for its first motions mechanism. Both models indicate that fault slip penetrates to depths of  $\sim 10$  km (a few kilometers short of the base of the aftershock zone), with peak slip at depths of 3–6 km. There are three discrete maxima of up to 5–6 m in the slip distribution associated with the Borrego, Pescadores and Indiviso faults. Across-strike profiles through along-strike horizontal displacements indicate shallow strike-slip components of up to 3–4 m, significantly smaller than the peak values at depth (*Wei et al.*, 2011).

Kinematic models, which take the fault geometries derived from geodesy and map the progression of slip from seismological data, reveal important additional properties of the rupture (*Wei et al.*, 2011; *Uchide et al.*, 2013). Slip initiated on an E-dipping normal segment before progressing bilaterally onto the Indiviso and Pescadores faults after 15–20 seconds. Strong high-frequency radiation  $\sim 50$  km NW of the hypocenter after  $\sim 28$  seconds may correspond to the step-over between the Borrego and Paso Superior faults, and starting at  $\sim 32$  seconds the Pescadores fault may have slipped a second time. Finally, rupture ceases simultaneously at the NW end of the Paso Superior fault and the SE end of the Indiviso fault after  $\sim 50$  seconds.

### 2.3 Field and lidar observations of surface rupturing

The earthquake generated  $\sim 120$  km of surface ruptures from the Colorado River delta in the SE to the US–Mexico border in the NW, in close correspondence with the aftershock zone. The surface rupture characteristics have been documented through extensive field measurements (*Gold et al.*, 2013; *Fletcher et al.*, 2014; *Teran et al.*, 2015) and also, for the first time ever, by analyzing lidar surveys undertaken before and after the earthquake (*Oskin et al.*, 2012). The pre-event lidar data belong to a regional survey by the Instituto Nacional de Estadística y Geografía (INEGI) in August 2006 whilst the post-event data were collected by the National Center for Airborne Laser Mapping (NCALM) in August 2010, four months after the earthquake (see Acknowledgments).

For  $\sim 50$  km SE of the epicenter, the newly identified Indiviso fault produced a zone of distributed fracturing and liquefaction within thick deltaic deposits of the Colorado River (*Fletcher et al.*, 2014). This surface expression is characteristic of earthquakes in the delta, such as the 1934 and 1980 events on the neighboring Cerro Prieto fault. Though the sense of slip can be estimated from the en echelon fracture arrangement, slip magnitude is difficult to determine from field measurements due to the lack of a discrete, laterally-continuous surface trace. However, elevation changes computed by subtracting pre-event from post-event lidar digital terrain models (DTMs) indicated up to 0.5 m of vertical displacement across the Indiviso fault zone, down to the SW (*Oskin et al.*, 2012). Lidar imagery was also used to reconstruct the geometry of faulted cultural features such as canal levees, which indicated  $\sim 0.5$  m of right-lateral displacement. Geodetic models imply peak slip at depth of  $\sim 2$ –5 m along much of the Indiviso fault (*Fialko et al.*, 2010; *Wei et al.*, 2011), so

it is clear that only a small proportion propagated into the near-surface.

North-west of the epicenter, the surface rupture enters the Sierra Cucapah (Figure 1b), an uplift composed of Mesozoic igneous and metamorphic rocks and Tertiary volcanics and sediments (Fletcher *et al.*, 2014). In the south-easternmost Sierra Cucapah, its trace follows two splays of the sub-vertical Laguna Salada fault over a distance of  $\sim 7$  km, with overall right-lateral slip of up to  $\sim 3$  m. Vertical displacements are limited to  $< 0.3$  m and change polarity along strike. The rupture then merges into the steeply NE-dipping Pescadores fault, which it follows for a further  $\sim 15$  km into the central Sierra Cucapah mountains, producing horizontal displacements of up to  $\sim 4$  m and vertical displacements of up to  $\sim 2$  m, now consistently down to the NE. This section of the rupture is difficult to discern in maps of lidar elevation change, any vertical displacements being obscured by the lateral offset of rugged topography (Oskin *et al.*, 2012).

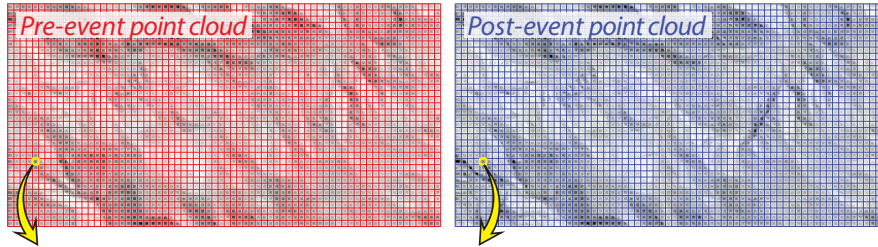
North-west of the Pescadores section, coseismic faulting steps left across a broad relay zone known as the Puerta Accommodation Zone (PAZ), eventually linking up with the Borrego fault  $\sim 10$  km to the NW. Though only a few scattered ruptures were identified on the ground and surface faulting is hard to discern from lidar elevation changes, pixel cross correlation results indicate a sharp, near-continuous horizontal displacement discontinuity crossing the PAZ (Wei *et al.*, 2011; Fletcher *et al.*, 2014). It is possible either that the surface trace of the rupture is largely obliterated by coseismic mass wasting, or that slip at depth failed to propagate upwards all the way to the surface. The Borrego fault itself dips moderately (as low as  $\sim 40^\circ$ ) towards the NE and accommodates up to  $\sim 3.5$  m of oblique normal-dextral slip across a typically  $> 50$  m-wide damage zone (Gold *et al.*, 2013; Fletcher *et al.*, 2014). A second relay zone known as the Paso Inferior accommodation zone (PIAZ) then links the Borrego fault with the Paso Superior fault to the North (Oskin *et al.*, 2012; Fletcher *et al.*, 2014). The PIAZ is characterized by discontinuous scarps in low-relief terrain bordering the Laguna Salada that represent a diverse range of faults, from low-angle ( $\sim 20^\circ$ ) NE-dipping detachments to steep, SW-dipping antithetic faults. In addition, lidar elevation changes appear to show kilometer-scale bending across the PIAZ, perhaps accounting for the extensive ground cracking that was observed even away from the main scarps.

North of the PIAZ, for a distance of  $\sim 10$  km, the surface rupture follows the trace of the NE-dipping Paso Superior detachment fault which juxtaposes Neogene sediments with Mesozoic crystalline basement (Fletcher *et al.*, 2014). Where well exposed, the surface rupture dips at angles as shallow as  $20^\circ$  and accommodates up to  $\sim 3.3$  m of oblique normal-dextral slip. The rupture terminates at its northern limit in scattered, conjugate NW-SE (dextral) and SE-SW (sinistral) fractures and N-S scarps in the low-relief terrain close to the US-Mexico border, which lies within the hanging-wall of the Paso Superior detachment. This is an area of intense aftershock activity, including the largest single aftershock (to date) of  $M_w$  5.7 (Hauksson *et al.*, 2011). UAVSAR imagery indicates that the earthquake also triggered minor ( $< 4$  cm) slip along the southern San Jacinto and Imperial faults to the north and east of the rupture termination (Donnellan *et al.*, 2014).

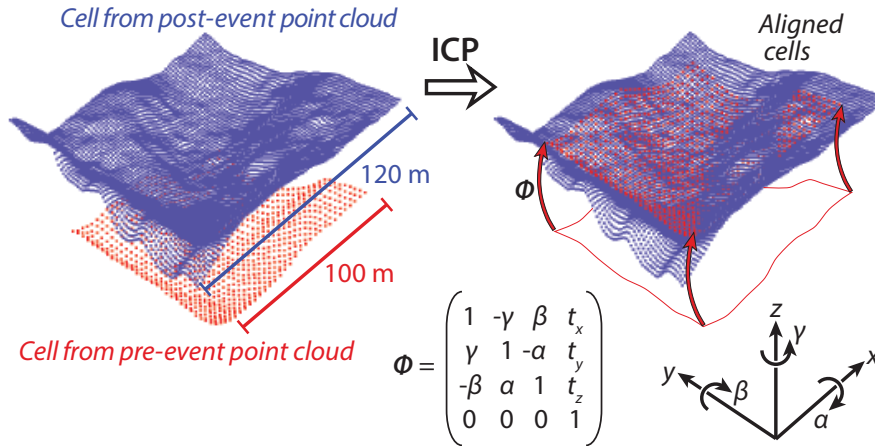
### 3 Three-dimensional lidar displacements

We computed the 3-D surface displacement field within the El Mayor-Cucapah rupture zone by differencing the pre- and post-event lidar point clouds using an adaptation of the Iterative Closest Point (ICP) algorithm (Nissen *et al.*, 2012). This procedure allows us to work directly with the irregular point clouds and copes well with their markedly differing densities, which average

**1** Split both datasets into square cells



**2** Take two equivalent cells and align with ICP



**3** Move on to next pair of cells and repeat step 2

Figure 2: Outline of our method for aligning pre- and post-event point cloud cells, based on an adaptation of the Iterative Closest Point (ICP) algorithm (Nissen et al., 2012). In step 2, the rigid body transformation  $\Phi$  that minimizes closest point distances between the pre- and post-event cells comprises translations  $t_x$ ,  $t_y$  and  $t_z$  in the  $x$ ,  $y$  and  $z$  directions, and rotations  $\alpha$ ,  $\beta$  and  $\gamma$  about the  $x$ ,  $y$  and  $z$  axes. This figure is modified from Nissen et al. (2014).

$\sim 0.013$  points/m<sup>2</sup> and  $\sim 10$  points/m<sup>2</sup> for the pre- and post-event datasets, respectively. Each point cloud is first separated into square cells with prescribed dimensions, and then each pre-event cell is aligned with its post-event equivalent by iteratively minimizing distances between closest point pairs using rigid-body translations and rotations (Figure 2). After testing, we found that a cell size of 100 m yielded robust displacements at an adequate resolution. However, insufficient topographic variation within a pair of cells results in a quasi-random alignment, leading in this instance to incoherent displacements within the Colorado River delta and Laguna Salada basin. We therefore restrict our analysis to the northern half of the rupture zone within the higher relief Sierra Cucapah. Initial results were also hampered by large N–S-trending artefacts related to errors in the pre-event survey data. Reprocessing of the pre-event lidar, described in Glennie et al. (2014), has reduced but not entirely eliminated these artefacts from the results presented here (Figure 3).

Sharp discontinuities in one or more of the  $x$  (E–W),  $y$  (N–S) and  $z$  (vertical) displacement fields (top row of panels in Figure 3) delineate the entire fault trace, including across the Puerta accommodation zone where we observe a hitherto undocumented vertical offset of  $\sim 1$ – $2$  m, up to the SW.

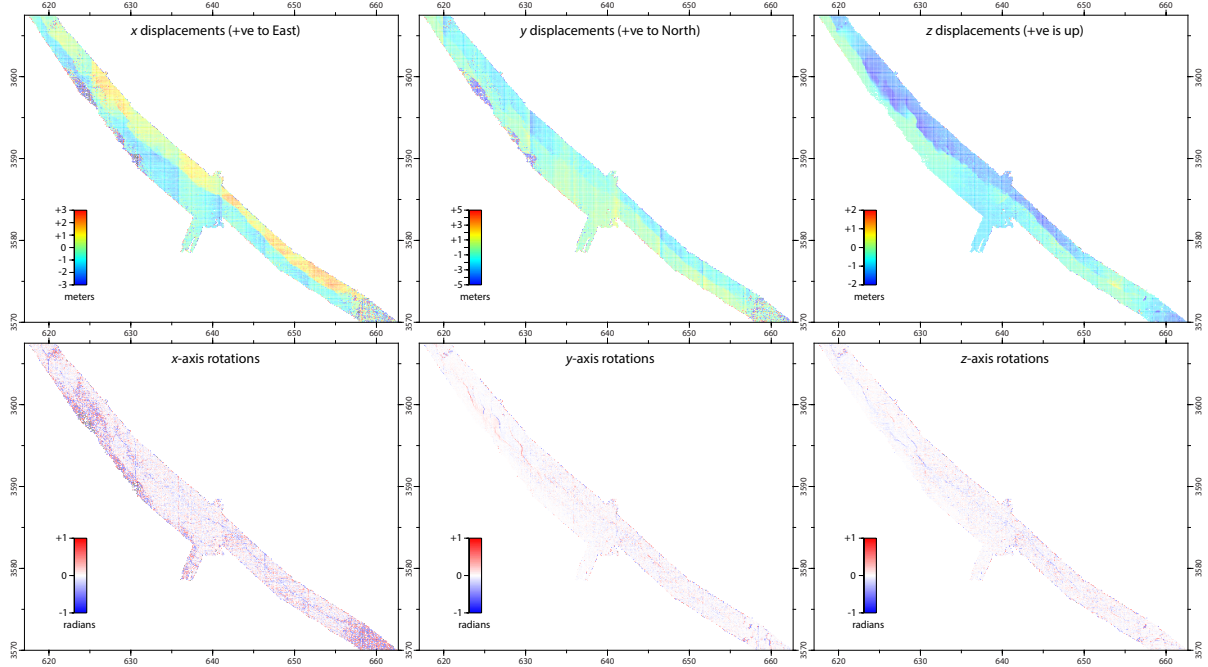


Figure 3: ICP results for a cell size of 100 m. The upper panels show translations in the  $x$ ,  $y$ , and  $z$  directions, with positive values indicating motion to the East, North, and up. The lower panels show rotations about the  $x$ ,  $y$  and  $z$  axes, with positive values indicating clockwise rotations about the positive axis direction (see Figure 2). Map extents are the same as in Figure 1b, marked with UTM zone 11 coordinates in km.

On close inspection the PAZ discontinuity has a scalloped appearance which may indicate accommodation of shear by distributed faulting and/or small-scale block rotations rather than by a single, through-going fault. Much of the rupture is also outlined by cells that contain significant rotations, reflecting attempted rigid body alignments in the presence of newly-formed surface scarps (lower row of panels in Figure 3). As expected, rotations about the  $y$  axis are positive (red) for NE-facing scarps and negative (blue) for SW-facing scarps, such as those in the northern Paso Inferior accommodation zone. Rotations about the  $z$  axis are everywhere negative, consistent with a right-lateral sense of shear within cells that capture the surface faulting. There is no continuous trace of cell rotations through the PAZ, consistent with an absence of discrete surface faulting within this relay zone.

Next we test for the involvement of low-angle normal faulting, as was proposed in the northern Sierra Cucapah on the basis of field mapping (Fletcher *et al.*, 2014; Teran *et al.*, 2015). In Figure 4, the  $x$  and  $y$  displacements are combined and rotated into horizontal motions parallel and perpendicular to the overall NW-SE fault trace. Absolute measurements of the along-strike or across-strike displacements are still hampered by the N-S-oriented survey artefacts, but their relative magnitudes either side of the fault trace can still be determined in most places. These differences represent the strike-slip and heave of the fault, respectively. The heave can then be compared with the throw, estimated from offsets in the vertical displacement field, which for ease of comparison are plotted again in the right-hand panel of Figure 4. Along the Pescadores and Borrego faults, and within the PAZ between them, fault throw appears significantly larger than heave, indicating that any normal component of slip is taken up by steeply-dipping faulting. However, further north-west, the extensional heave exceeds the vertical throw along a  $\sim 5$  km section of the Paso Superior fault, which

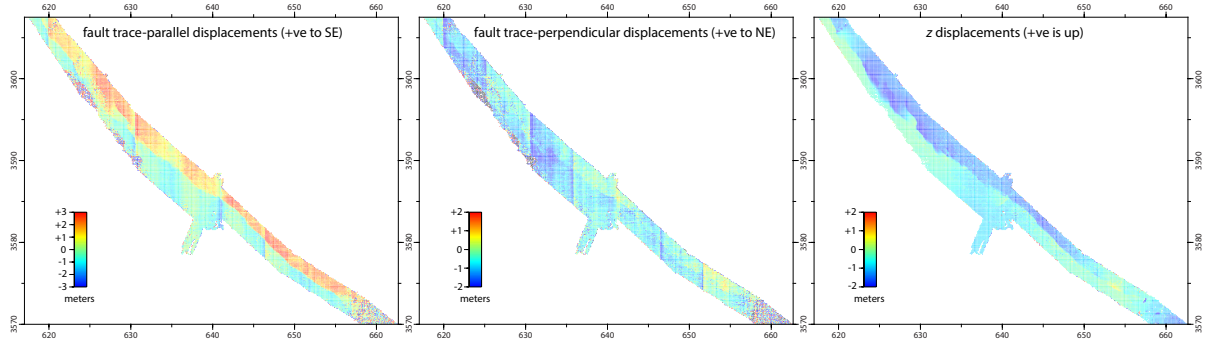


Figure 4: *ICP displacements parallel to the overall NW–SE fault trace (left panel) and perpendicular to it (center panel), derived from the  $x$  and  $y$  displacements in Figure 3. Vertical displacements are shown again for comparison (right panel), with the same color saturation as for the fault trace-perpendicular displacements.*

encompasses some of the key field localities in which low-angle slip was observed on the ground (Fletcher *et al.*, 2014; Teran *et al.*, 2015). The lidar displacements therefore confirm that locally, slip on the low-angle Paso Superior detachment fault extends into the subsurface underneath the north-eastern part of the lidar footprint (i.e. over a distance of  $\sim 2$  km from the surface trace).

Existing seismological and geodetic models of the El Mayor-Cucapah earthquake therefore fail to capture genuine shallow-angle slip in the northern rupture zone. However, it is possible that they instead accurately characterize the deeper part of the fault zone, which may not be well-sampled by the narrow ( $\sim 3$  km-wide) lidar swath (Fialko *et al.*, 2010; Wei *et al.*, 2011). We note that aftershock locations and mechanisms in this region appear inconsistent with deep slip on a NE-ward extension of the Paso Superior fault beneath the Mexicali Valley (Hauksson *et al.*, 2011).

## 4 Conclusions

This award has supported development of methods to compute three-dimensional surface displacements from ‘before’ and ‘after’ high-resolution topography datasets. Applied here to the 2010 El Mayor-Cucapah earthquake, we help resolve discrepancies between published fault models based on field measurements and those based on seismology and satellite geodesy. The El Mayor-Cucapah rupture mostly involved steeply-dipping faulting, with vertical slip generally exceeding extensional slip within the Sierra Cucapah mountains. However, we do also find evidence for subsurface normal slip on the low-angle Paso Superior detachment fault in the northernmost rupture zone, consistent with local field measurements of surface offsets.

## 5 Acknowledgments

This research was supported by the U.S. Geological Survey (USGS), Department of the Interior, under USGS award G12AC20042 to Edwin Nissen. The views and conclusions contained in this document are those of the author and should not be interpreted as necessarily representing the official policies, either expressed or implied, of the U.S. Government. The author wishes to thank collaborators Ramon Arrowsmith, Srikanth Saripalli and Aravindhan Krishnan at Arizona State University, Michael Oskin at the University of California Davis, Craig Glennie at the University of

Houston and the National Center for Airborne Laser Mapping (NCALM), and Alejandro Hinojosa-Corona at CISESE Ensenada, for their help on this project. Initial analysis of El Mayor-Cucapah lidar data was supported by a National Science Foundation (NSF) collaborative research grant (EAR 1148319), whilst complementary work on lidar differencing has been further supported by a grant from the Southern California Earthquake Center (SCEC award 14101). The author thanks the Instituto Nacional de Estadística y Geografía (INEGI) for making the pre-event lidar survey available, NCALM for flying the post-earthquake survey, and the NSF-supported Open Topography facility (awards 1226353 and 1225810) for publicly hosting both datasets.

## References

- Abers, G. A. (1991), Possible seismogenic shallow-dipping normal faults in the Woodlark-D'Entrecasteaux extensional province, Papua New Guinea, *Geology*, *19*, 1205–1208.
- Axen, G. J. (1999), Low-angle normal fault earthquakes and triggering, *Geophys. Res. Lett.*, *26*, 3693–3696.
- Axen, G. J., J. M. Fletcher, E. Cowgill, M. Murphy, P. Kapp, I. MacMillan, E. Ramos-Velázquez, and J. Aranda-Gómez (1999), Range-front fault scarps of the Sierra El Mayor, Baja California: Formed above an active low-angle normal fault?, *Geology*, *27*, 247–250.
- Castro, R. R., J. G. Acosta, V. M. Wong, A. Perez-Vertti, A. Mendoza, and L. Inzunza (2011), Location of Aftershocks of the 4 April 2010 Mw 7.2 El Mayor-Cucapah Earthquake of Baja California, Mexico, *Bull. Seismol. Soc. Am.*, *101*(6), 3072–3080.
- Donnellan, A., J. Parker, S. Hensley, M. Pierce, J. Wang, and J. Rundle (2014), UAVSAR observations of triggered slip on the Imperial, Superstition Hills, and East Elmore Ranch Faults associated with the 2010 M 7.2 El Mayor-Cucapah earthquake, *Geochem. Geophys. Geosyst.*, *15*, 815–829.
- Fialko, Y., A. Gonzalez, J. J. Gonzalez-Garcia, S. Barbot, S. Leprince, D. T. Sandwell, and D. C. Agnew (2010), Static Rupture Model of the 2010 M7.2 El Mayor-Cucapah Earthquake from ALOS, ENVISAT, SPOT and GPS Data, *AGU Fall Meeting Abstr.*, p. B2125.
- Fletcher, J. M., and R. M. Spelz (2009), Patterns of Quaternary deformation and rupture propagation associated with an active low-angle normal fault, Laguna Salada, Mexico: Evidence of a rolling hinge?, *Geosphere*, *5*, 385–407.
- Fletcher, J. M., O. J. Teran, T. K. Rockwell, M. E. Oskin, K. W. Hudnut, K. J. Mueller, R. M. Spelz, S. O. Akciz, E. Masana, G. Faneros, E. J. Fielding, S. Leprince, A. E. Morelan, J. Stock, D. K. Lynch, A. J. Elliott, P. Gold, J. Liu-Zeng, A. Gonzalez-Ortega, A. Hinojosa-Corona, and J. Gonzalez-Garcia (2014), Assembly of a large earthquake from a complex fault system: Surface rupture kinematics of the 4 April 2010 El Mayor-Cucapah (Mexico) Mw 7.2 earthquake, *Geosphere*, *10*(4), 797–827.
- Glennie, C. L., A. Hinojosa-Corona, E. Nissen, A. Kusari, M. E. Oskin, J. R. Arrowsmith, and A. Borsa (2014), Optimization of legacy lidar data sets for measuring near-field earthquake displacements, *Geophys. Res. Lett.*, *41*, 3494–3501.

- Gold, P. O., M. E. Oskin, A. J. Elliott, A. Hinojosa-Corona, M. H. Taylor, O. Kreylos, and E. Cowgill (2013), Coseismic slip variation assessed from terrestrial lidar scans of the El Mayor-Cucapah surface rupture, *Earth Planet. Sci. Lett.*, *366*, 151–162.
- Gonzalez-Ortega, A., D. Fialko, Y. and Sandwell, F. Alejandro Nava-Pichardo, J. Fletcher, J. Gonzalez-Garcia, B. Lipovsky, M. Floyd, and G. Funning (2014), El Mayor-Cucapah ( $M_w$  7.2) earthquake: Early near-field postseismic deformation from InSAR and GPS observations, *J. Geophys. Res.*, *119*, 1482–1497.
- Hauksson, E., J. Stock, K. Hutton, W. Yang, J. A. Vidal-Villegas, and H. Kanamori (2011), The 2010  $M_w$  7.2 El Mayor-Cucapah Earthquake Sequence, Baja California, Mexico and Southernmost California, USA: Active Seismotectonics along the Mexican Pacific Margin, *Pure. Appl. Geophys.*, *168*, 1255–1277.
- Hough, S. E., and A. J. Elliot (2004), Revisiting the 23 February 1892 Laguna Salada Earthquake, *Bull. Seismol. Soc. Am.*, *94*, 1571–1578, doi:10.1785/012003244.
- Jackson, J. A., and N. J. White (1989), Normal faulting in the upper continental crust: observations from regions of active extension, *J. Struct. Geol.*, *11*, 15–36.
- Mueller, K., G. Kier, T. Rockwell, and C. H. Jones (2009), Quaternary rift flank uplift of the Peninsular Ranges in Baja and southern California by removal of mantle lithosphere, *Tectonics*, *28*, TC5003.
- Mueller, K. J., and T. K. Rockwell (1995), Late quaternary activity of the Laguna Salada fault in northern Baja California, Mexico, *Geol. Soc. Am. Bull.*, *107*, 8–18.
- Nagy, E. A., and J. M. Stock (2000), Structural controls on the continent-ocean transition in the northern Gulf of California, *J. Geophys. Res.*, *105*, 16,251–16,269.
- Nissen, E., A. K. Krishnan, J. R. Arrowsmith, and S. Saripalli (2012), Three-dimensional surface displacements and rotations from differencing pre- and post-earthquake LiDAR point clouds, *Geophys. Res. Lett.*, *39*, L16301.
- Nissen, E., T. Maruyama, J. Ramon Arrowsmith, J. R. Elliott, A. K. Krishnan, M. E. Oskin, and S. Saripalli (2014), Coseismic fault zone deformation revealed with differential lidar: Examples from Japanese  $M_w \sim 7$  intraplate earthquakes, *Earth Planet. Sci. Lett.*, *405*, 244–256.
- Oskin, M. E., J. R. Arrowsmith, A. H. Corona, A. J. Elliott, J. M. Fletcher, E. J. Fielding, P. O. Gold, J. J. G. Garcia, K. W. Hudnut, J. Liu-Zeng, and O. J. Teran (2012), Near-Field Deformation from the El Mayor-Cucapah Earthquake Revealed by Differential LIDAR, *Science*, *335*, 702–705.
- Proffett, J. M. (1977), Cenozoic geology of the Yerington district, Nevada, and implications for the nature and origin of Basin and Range faulting, *Geol. Soc. Am. Bull.*, *88*, 247–266.
- Styron, R. H., and E. A. Hetland (2014), Estimated likelihood of observing a large earthquake on a continental low-angle normal fault and implications for low-angle normal fault activity, *Geophys. Res. Lett.*, *41*, 2342–2350.
- Suárez-Vidal, F., L. Munguía-Orozco, M. González-Escobar, J. González-García, and E. Glowacka (2007), Surface rupture of the Morelia fault near the Cerro Prieto geothermal field, Mexico,

- Baja California, Mexico, during the Mw 5.4 earthquake of 24 May 2006, *Seismol. Res. Lett.*, *78*(3), 394–399.
- Teran, O., J. M. Fletcher, M. E. Oskin, T. K. Rockwell, K. W. Hudnut, R. M. Spelz, S. O. Akciz, A. P. Hernandez-Flores, and A. E. Morelan (2015), Geologic and structural controls on rupture zone fabric: A field-based study of the 2010 Mw 7.2 El Mayor-Cucapah earthquake surface rupture, *Geosphere*, *11*(3), 899–920.
- Trugman, D. T., A. A. Borsa, and D. T. Sandwell (2014), Did stresses from the Cerro Prieto Geothermal Field influence the El Mayor-Cucapah rupture sequence?, *Geophys. Res. Lett.*, *41*, 8767–8774.
- Uchide, T., H. Yao, and P. M. Shearer (2013), Spatio-temporal distribution of fault slip and high-frequency radiation of the 2010 El Mayor-Cucapah, Mexico earthquake, *J. Geophys. Res.*, *118*, 1546–1555.
- Wei, S., E. Fielding, S. Leprince, A. Sladen, J.-P. Avouac, D. Helmberger, E. Hauksson, R. Chu, M. Simons, K. Hudnut, T. Herring, and R. Briggs (2011), Superficial simplicity of the 2010 El Mayor-Cucapah earthquake of Baja California in Mexico, *Nat. Geosci.*, *4*, 615–618.
- Wernicke, B. (1995), Low-angle normal faults and seismicity: A review, *J. Geophys. Res.*, *100*, 159–20,174.
- Zheng, Y., J. Li, Z. Xie, and M. H. Ritzwoller (2012), 5Hz GPS seismology of the El Mayor-Cucapah earthquake: estimating the earthquake focal mechanism, *Geophys. J. Int.*, *190*, 1723–1732.